

# APPLICATION OF EXTENDED QUADRATURE METHOD OF MOMENTS FOR SIMULATION OF BUBBLY FLOW AND MASS TRANSFER IN GAS-LIQUID STIRRED TANKS

Ehsan Askari,<sup>ID\*</sup> Gabriel St-Pierre Lemieux and Pierre Proulx

Chemical Engineering Department, Sherbrooke University, Sherbrooke, QC, Canada

In the present paper, two gas-liquid stirred tanks, one agitated by a radial impeller and another by an axial impeller, are modelled using the open-source computational fluid dynamic (CFD) package OpenFOAM (open source field operation and manipulation). The combined effect of the bubble break-up and coalescence in the tank is considered by a population balance model (PBM) called extended quadrature method of moments (EQMOM). The three-dimensional simulation is made using a multiple reference frame (MRF), a well-established method for the modelling of mixers. Dispersed gas and bubble dynamics in the turbulent flow are modelled using the Eulerian-Eulerian approach (E-E) with mixture k-epsilon turbulent model and the modified Tomiyama drag coefficient for the momentum exchange. The model is developed to predict the spatial distribution of gas phase fraction, Sauter mean bubble diameter ( $d_{32}$ ), number density function (NDF), dissolved oxygen (DO) evolution, and flow structure. The numerical results are compared with experimental data and a fair agreement is achieved. The results of the axial impeller are discussed based on four impeller rotational speeds with different volumetric mass transfer coefficients.

**Keywords:** CFD-PBM, EQMOM, mass transfer, gas-liquid flow, stirred tank

## INTRODUCTION

Mixing of gas-liquid systems is important in numerous processes such as absorption, desorption, flotation, and biochemical fermentations. A good interfacial contact area between gas and liquid obtained by effective and efficient mixing is required to maximize the mass transfer. The modelling of the complex flow in mixing devices is a formidable computational challenge. Although computational fluid dynamics (CFD) methods have significantly advanced with significant contributions from fundamental and applied research in the last 30 years, it still remains a difficult task to use these methods to help in the design and analysis of stirred tanks. The scientific and technical literature on the subject has rapidly evolved from single phase rotating impeller systems (Luo et al.,<sup>[1]</sup> Tabor et al.,<sup>[2]</sup> Micale et al.,<sup>[3]</sup> Holzinger,<sup>[4]</sup> and Lane et al.<sup>[5]</sup>) to population balance methods aiming at the prediction of the disperse phase bubble sizes (Luo et al.,<sup>[1]</sup> Venneker et al.,<sup>[6]</sup> Kerdouss et al.,<sup>[7-9]</sup> Lane et al.,<sup>[5,10]</sup> Gimbut et al.,<sup>[11]</sup> and Holzinger<sup>[4]</sup>).

According to research literature, the gas-liquid stirred vessels can be modelled simpler to study overall parametric analysis, or more complicated to explain the bubble size distribution. The single bubble size models can yield results with less computational demand providing a local description of two-phase flow (Deen et al.,<sup>[12]</sup> Friberg,<sup>[13]</sup> Morud and Hjertager,<sup>[14]</sup> Ranade and Deshpande,<sup>[15]</sup> and Ranade<sup>[16]</sup>). However, this type of model cannot provide reliable information for industrial designs (Kresta et al.<sup>[17]</sup>). The prediction of bubble size distribution is an important problem in the modelling of multiphase dispersion. Local monodisperse models in addition to the phase continuity equation can globally account for polydispersity of the bubbles. As local monodisperse models yield a non-constant bubble size, the disperse phase is local monodisperse with a locally constant diameter of the particles (Kerdouss et al.<sup>[7]</sup> and Ishii et al.<sup>[18]</sup>). However, this approach does not consider the local probability distribution of the bubble size. The models obtain more information

on the dispersed phase pattern covering the details of bubble polydispersity (Dhanasekharan et al.<sup>[19]</sup> and Venneker et al.<sup>[6]</sup>). The most-used methods of locally polydisperse models are the classes method (CM) (Balakin et al.,<sup>[20]</sup> Bannari et al.,<sup>[21]</sup> Becker et al.,<sup>[22]</sup> Kumar and Ramkrishna,<sup>[23,24]</sup> and Puel et al.<sup>[25]</sup>), quadrature method of moments (QMOM) (McGraw,<sup>[26]</sup> Marchisio et al.,<sup>[27-29]</sup> and Sanyal et al.<sup>[30]</sup>), and direct quadrature method of moments (DQMOM) (Silva and Lage,<sup>[31]</sup> Selma et al.,<sup>[32]</sup> and Marchisio and Fox<sup>[33]</sup>).

The MUSIC (multisize group) model of CM developed by Helmholtz-Zentrum Dresden-Rossendorf (HZDR)<sup>[34]</sup> for gas-liquid systems has recently become a favourite choice and was released in the latest versions of Open Source CFD Toolbox (OpenFOAM). CM is intuitive and accurate, while computationally intensive. The higher computational cost comes from the large number of classes required to discretize the number density function (NDF). Additionally, this method needs the user to input a bubble size range to solve the population balance equation (PBE).

Compared with CM, QMOM solves fewer equations with a broad range of bubble size. However, if the value of the NDF for null internal coordinates requires to be calculated, QMOM method cannot be a good choice. Another limitation of QMOM is the use of the summation of Dirac delta functions to reconstruct NDF. This problem can arise through the simulation of combustion systems as well as dissolution processes due to two-phase mass transfer. The equations of weights and abscissas are directly solved in DQMOM method, although the failure related to non-conservative quantities for weights

\*Author to whom correspondence may be addressed.

E-mail address: ehsan.askari@usherbrooke.ca

Can. J. Chem. Eng. 97:2548–2564, 2019

© 2019 Canadian Society for Chemical Engineering

DOI 10.1002/cjce.23470

Published online 17 July 2019 in Wiley Online Library (wileyonlinelibrary.com).

and abscissas affects DQMOM (Yuan et al.<sup>[35]</sup>). To tackle the issues, Yuan et al.<sup>[35]</sup> developed an extended quadrature method of moments (EQMOM), which reconstructs NDF from a moment set using continuous kernel density functions instead of Dirac delta functions. Moreover, Madadi-Kandjani and Passalacqua<sup>[36]</sup> concluded from the EQMOM technique control that the reconstructed NDF generates realizable moments. The moments equations based on EQMOM involves transport by convection and source/sink terms for the coalescence or the break-up.

Locally polydisperse population balance models have been recently applied to model stirred tanks. Gao et al.<sup>[37]</sup> simulated droplet breakage in turbulent liquid-liquid dispersion by using a two-fluid model and QMOM method implemented in a CFD open-source package (OpenFOAM). They focused on breakage kernels corresponding to several different test cases. Their model predictions were validated against experimental data. Li et al.<sup>[38]</sup> compared EQMOM with QMOM in a turbulent liquid-liquid mixing and they found these two approaches make similar predictions. They performed reconstruction of the droplet size distribution with the use of EQMOM. Gimbut et al.<sup>[11]</sup> developed a CFD-QMOM mass transfer model to simulate gas-liquid stirred vessels with presence of Rushton propeller. Their model was established for a high-speed mixing. In such circumstances, the convective and diffusion terms can be ignored. Hence, their comparison was based on overall two-phase mass transfer coefficient. In their PBM model (QMOM), the convective term was removed in physical space. Kerdouss et al.<sup>[8]</sup> reported the same approach but in a different stirred tank reactor called the laboratory scale New Brunswick BioFlo using the class method (CM). These two studies prove the monodispersity of the bubbles is not a precise choice in gas-liquid stirred mixers and the population balance model (PBM) achieves the real physics of the system and gives more accurate output.

The previous work (Askari et al.<sup>[39]</sup>) provided a comparison of computational time for different PBM methods, including DQMOM, QMOM, CM, and EQMOM applied in bubble columns. The results demonstrated the CFD-PBM using EQMOM provides a fair prediction in bubbly flow devices as well as CM with numerous classes but needs less computational effort compared with CM. This investigation indicated that EQMOM is more expensive than QMOM in terms of computational cost. However, the advantage is the reconstruction of the continuous NDF with the same number of nodes.

In the present investigation, the combined computational fluid dynamics (CFD) and population balance model (PBM) approach is applied on two mixer tanks. The first case is a gas-liquid stirred tank containing a radial impeller, the so-called Rushton reactor. The second one is a laboratory scale (3 L) New Brunswick bioreactor agitated by an axial impeller. The experimental set-up corresponds to the ones used by Kerdouss et al.<sup>[8]</sup> for the axial impeller and Deen et al.<sup>[12]</sup> for the Rushton turbine. The CFD-PBM solver is used using EQMOM to reconstruct the bubble size distribution in liquid phase. In this study, EQMOM was, to the authors' knowledge, for the first time implemented in the CFD code OpenFOAM to simulate coalescence and breakage of gas-liquid systems in stirred tanks. Moreover, the equation of oxygen mass fraction is solved in a bioreactor simulation by the developed CFD-PBM OpenFOAM solver to achieve the concentration distribution of oxygen as the dissolved component in water. The implementation and use of EQMOM with a log-normal NDF in a two phase CFD solver based on open source CFD code OpenFOAM and study of dissolved oxygen evolution are the main novelties of this study. The principal goal of the present paper relies on the application of EQMOM in the gas-liquid stirred tank,

which leads us to achieve and investigate the continuous bubble size distribution for different speeds of rotation.

The paper is organized as follows. First, the experimental measurements conditions are described. Then the modelling method is explained. After that modelling results are validated by comparing them to experimental data. The simulation results are presented and discussed afterwards.

## EXPERIMENTAL SETUP

A Rushton stirred tank with a volume of 14 L, studied by Gimbut et al.,<sup>[11]</sup> was selected for the CFD-PBM modelling of an air-water flow with the presence of a radial impeller. The reader is referred to Gimbut et al.'s study<sup>[11]</sup> for the configuration details. For the second case, a 3 L New Brunswick BioFlo 110 bioreactor is equipped with a three bladed marine propeller. The blade is designed with a 45° angle and forms a total diameter of 7.1 cm, when the total diameter of the reactor is 12.5 cm. The impeller is located on a 1 cm shaft, where the furthest point of the impeller is placed 22 cm under the head plate of the 25 cm tall reactor. The sparger is placed close to the impeller at merely 5 cm under its centre including six holes with diameter of 0.1 cm. An polarographic-membrane oxygen probe (Inpro 6800 from Mettler Toledo) was used to track the dissolved oxygen concentration in the reactor. Nitrogen gas was used to de-aerate the reactor below the probe capacity. At this point, the air was diffused into the reactor until saturation was reached.

In the present research, numerical simulations are discussed and compared to the experimental measurements at a temperature of 20 °C in a stirred tank. Mixer is filled up to a height  $H = 4/3T$  with tap water and sparged with gas flow rate of  $2.3 \cdot 10^{-5} \text{ m}^3 \cdot \text{s}^{-1}$  for bioreactor and 0.7 VVM for Rushton impeller. Four impeller rotation speeds of 50, 150, 300, and 600 rpm corresponding, respectively, to Reynolds number,  $Re = \rho_L ND^2 / \mu_L \approx 2.8 \times 10^4$  to  $3.5 \times 10^5$ , for the bioreactor and one rotation speed of 513 rpm for the radial impeller in the Rushton mixer are applied. According to the applied rotational speeds of the bioreactor and Rushton turbine, the calculated Reynolds numbers are more than the critical ones reported in the literature for mixers. The water properties are set as  $\rho_L = 998.2 \text{ kg} \cdot \text{m}^{-3}$ ,  $\mu_L = 0.000\ 89 \text{ kg} \cdot \text{m}^{-1} \cdot \text{s}^{-1}$ , and  $\sigma = 0.073 \text{ N} \cdot \text{m}^{-1}$ . The properties of air are set as  $\rho_G = 1.225 \text{ kg} \cdot \text{m}^{-3}$  and  $\mu_G = 1.789 \cdot 10^{-5} \text{ kg} \cdot \text{m}^{-1} \cdot \text{s}^{-1}$ .

## NUMERICAL MODEL

### Governing Flow Equations

In the Euler-Euler approach, the existing phases are treated as interpenetrating continuum and the velocity and pressure fields of the gas phase and liquid phase are solved as well as their volume fractions along the mixture k-epsilon turbulence model. The mathematical form of two-fluid equations resembles the single phase Navier-Stokes equations but the two-fluid equations contain a term referred to mass and momentum exchange between phases. The continuity equation for the volume fraction of the dispersed phase is written as:

$$\frac{\partial}{\partial t} (\rho_G \alpha_G) + \nabla \cdot (\alpha_G \rho_G \vec{U}_G) = 0 \quad (1)$$

where  $\rho_G$ ,  $\alpha_G$ , and  $\vec{U}_G$  represent the density, volume fraction, and average velocity, respectively, of the dispersed phase (gas). The

continuous phase (liquid)  $L$  and the gas phase  $G$  are assumed to share the space in proportion to their volume such that their volume fractions sum to unity in the cell domain. Hence, the volume fraction of the continuous phase  $\alpha_L$  is calculated by:

$$\alpha_L + \alpha_G = 1.0 \quad (2)$$

The momentum conservation equation for the phase  $i$  after averaging is written as:

$$\frac{\partial}{\partial t}(\rho_i \alpha_i \vec{U}_i) + \nabla \cdot (\alpha_i \rho_i \vec{U}_i \vec{U}_i) = -\alpha_i \nabla p + \nabla \cdot \vec{\tau}_{\text{effi}} + \vec{R}_i + \vec{F}_i + \alpha_i \rho_i \vec{g} \quad (3)$$

$p$  is the pressure shared by the two phases and  $\vec{R}_i$  are the interphase momentum exchange terms. The term  $\vec{F}_i$  expresses the Coriolis and centrifugal forces applied in the rotating reference frame for the MRF model which is written as:

$$\vec{F}_i = -2\alpha_i \rho_i \vec{N} \times \vec{U}_i - \alpha_i \rho_i \vec{N} \times (\vec{N} \times \vec{r}) \quad (4)$$

The Reynolds stress tensor  $\vec{\tau}_{\text{effi}}$  is related to the mean velocity gradients using Boussinesq hypothesis:

$$\begin{aligned} \vec{\tau}_{\text{effi}} &= \alpha_i (\mu_{\text{lam},i} + \mu_{\text{t},i}) (\nabla \vec{U}_i + \nabla \vec{U}_i^T) \\ &- \frac{2}{3} \alpha_i (\rho_i k_i + (\mu_{\text{lam},i} + \mu_{\text{t},i}) \nabla \cdot \vec{U}_i) \vec{I} \end{aligned} \quad (5)$$

#### Interfacial Momentum Exchange

The most important interfacial force is the drag force acting on the bubbles resulting from the mean relative velocity between the two phases. Other forces such as lift and turbulent dispersion may in some instances be significant under the velocity gradient of the surrounding liquid and acceleration of bubbles, respectively. Both these forces have not been included in the present study. Scargiali et al.<sup>[40]</sup> reported that turbulent dispersion and lift force are almost negligible in gas-liquid stirred tanks. The term  $\vec{R}_i$  is reduced only to the drag force proportional to the mean velocity difference, given by the following form:

$$\vec{R}_L = -\vec{R}_G = K (\vec{U}_G - \vec{U}_L) \quad (6)$$

$K$  is the liquid-gas exchange coefficient written as:

$$K = \frac{3}{4} \rho_L \alpha_L \alpha_G \frac{C_D}{d} |\vec{U}_G - \vec{U}_L| \quad (7)$$

Here,  $d$  is the bubble diameter.

For calculation of the drag coefficient, the standard correlation of Tomiyama et al.<sup>[41]</sup> is used to take into account the bubble shape and tap water as fully contaminated liquid:

$$C_D = \max \left\{ \frac{24}{Re_p} \left( 1 + 0.15 Re_p^{0.687} \right), \frac{8}{3} \frac{Eo}{Eo + 4} \right\} \quad (8)$$

where  $Re_p$  is the relative Reynolds number and  $Eo$  is the Eotvos number. The current form of drag model takes into account the

effect of turbulence in the liquid phase using the definition of Equation (9):<sup>[42]</sup>

$$Re_p = \frac{\rho_L |\vec{U}_G - \vec{U}_L| d}{\mu_L + C \mu_{t,L}} \quad (9)$$

Here,  $C$  is set to 0.3 for capturing the effect of the turbulence.<sup>[7]</sup> The Eotvos number is the ratio of buoyancy force to surface tension and is formulated as:

$$Eo = \frac{g(\rho_L - \rho_G)d^2}{\sigma} \quad (10)$$

#### Turbulence Model Equations

When the secondary phase is not dilute, the primary and secondary phases tend to fluctuate as one entity at high phase fractions. The use of one set of equations for  $k$  and  $\epsilon$  is suggested for the mixture of the continuous and disperse phases.<sup>[43]</sup>

The transport equations for the  $k_m$  and  $\epsilon_m$  are:

$$\begin{aligned} \frac{\partial}{\partial t}(\rho_m k_m) + \nabla \cdot (\rho_m \vec{U}_m k_m) &= \nabla \cdot \left( \frac{\mu_{t,m}}{\sigma_k} \nabla k_m \right) \\ &+ P_k^m - \rho_m \epsilon_m + S_k^m \end{aligned} \quad (11)$$

$$\begin{aligned} \frac{\partial}{\partial t}(\rho_m \epsilon_m) + \nabla \cdot (\rho_m \vec{U}_m \epsilon_m) &= \nabla \cdot \left( \frac{\mu_{t,m}}{\sigma_\epsilon} \nabla \epsilon_m \right) + \frac{\epsilon_m}{k_m} (C_{1\epsilon} P_k^m - C_{2\epsilon} \rho_m \epsilon_m) + C_{2\epsilon} \frac{\epsilon_m}{k_m} S_k^m \end{aligned} \quad (12)$$

where  $m$  refers to the mixture of the two phases.  $G_{KL}$  is the rate of production of turbulent kinetic energy. Further details about the definition of the model parameters are provided by Behzadi et al.<sup>[43]</sup>

#### Population Balance Models and CFD Implementation

Bubble size distribution is an essential parameter in CFD modelling of gas-liquid reactors to calculate the volumetric mass transfer coefficient and interphase momentum exchange. In the stirred tank, the flow is complex as gas bubbles break-up and coalesce due to their collision with eddies through the liquid phase. The eddies that are large enough to overcome the surface tension of the bubble act as a source of disruptive forces in the liquid and occur breakage. Bubbles can collide due to the random motion in a turbulent flow and hence the coalescence takes place. In the current approach, the reason for the change in bubble number density  $n$  is breakage and coalescence events using the EQMOM method with log-normal kernel density function. The number density function (NDF) is written as:<sup>[37,44]</sup>

$$\frac{\partial n}{\partial t} + \nabla \cdot (\vec{U}_G n) = B_{ag} - D_{ag} + B_{br} - D_{br} \quad (13)$$

where  $n$  is the number of bubbles per unit volume, and  $B_{br}$  and  $B_{ag}$  are the birth rates due to break-up and coalescence, respectively. The corresponding death rates are  $D_{br}$  and  $D_{ag}$ .

The breakage and coalescence source terms are modelled as (Marchisio et al.<sup>[27,28]</sup>):

$$B_{ag} = \frac{\zeta^2}{2} \int_0^\zeta \frac{\beta((\zeta^3 - \zeta'^3)^{1/3}, \zeta')}{(\zeta^3 - \zeta'^3)^{2/3}} n((\zeta^3 - \zeta'^3)^{1/3}; \mathbf{x}, t) \times n(\zeta'; \mathbf{x}, t) d\zeta' \quad (14)$$

$$D_{ag} = n(\zeta; \mathbf{x}, t) \int_0^\infty \beta(\zeta, \zeta') n(\zeta'; \mathbf{x}, t) d\zeta' \quad (15)$$

$$B_{br} = \int_\zeta^\infty a(\zeta') b(\zeta|\zeta') n(\zeta; \mathbf{x}, t) d\zeta' \quad (16)$$

$$D_{br} = a(\zeta) n(\zeta; \mathbf{x}, t) \quad (17)$$

Here,  $\beta(\zeta, \zeta')$  is the coalescence rate between bubbles of size  $\zeta$  and  $\zeta'$ ;  $a(\zeta)$  is the break-up frequency of a bubble with size  $\zeta$ ;  $b(\zeta|\zeta')$  represents daughter distribution function generated from the break-up of a bubble of size  $\zeta'$ .

The EQMOM method requires the moment transport equation to be obtained from the NDF equation. The moment definition of order  $k$  of the NDF is:

$$M_k = \int_0^{+\infty} n(L; \mathbf{x}, t) L^k dL \quad (18)$$

If the moment definition is applied to NDF equation, it leads to:

$$\frac{\partial M_k(t, x)}{\partial t} + \nabla \cdot (\vec{U}_G M_k(t, x)) = B_{ag,k} - D_{ag,k} + B_{br,k} - D_{br,k} \quad (19)$$

Since the NDF is unknown, it is approximated from the transport moments. Yuan et al.<sup>[35]</sup> approximated the NDF with a weighted sum of non-negative kernel density functions  $\delta_{\sigma(NDF)}(L, L_\alpha)$ :

$$n(L) \approx p_N(L) = \sum_{\alpha=1}^N W_\alpha \delta_{\sigma(NDF)}(L, L_\alpha) \quad (20)$$

where  $W_\alpha$  is the non-negative weight of each kernel density function,  $L_\alpha$  is the corresponding quadrature abscissae,  $N$  is the number of kernel density functions to approximate the NDF and  $\sigma_{(NDF)}$  is the variance of the distribution function (NDF).

The coupling with the E-E model is done via the Sauter mean diameter:

$$d_{32} = \frac{m_3}{m_2} \quad (21)$$

#### Source terms in the moment transport equations

$$B_{ag,k} = \frac{1}{2} \sum_{\alpha_1=1}^N \sum_{\beta_1=1}^{N_\alpha} W_{\alpha_1} W_{\alpha_1 \beta_1} \times \sum_{\alpha_2=1}^N \sum_{\beta_2=1}^{N_\alpha} W_{\alpha_2} W_{\alpha_2 \beta_2} (L_{\alpha_1 \beta_1}^3 + L_{\alpha_2 \beta_2}^3)^{k/3} a_{\alpha_1 \beta_1 \alpha_2 \beta_2} \quad (22)$$

$$D_{ag,k} = \sum_{\alpha_1=1}^N \sum_{\beta_1=1}^{N_\alpha} L_{\alpha_1 \beta_1}^k W_{\alpha_1} W_{\alpha_1 \beta_1} \sum_{\alpha_2=1}^N \sum_{\beta_2=1}^{N_\alpha} W_{\alpha_2} W_{\alpha_2 \beta_2} a_{\alpha_1 \beta_1 \alpha_2 \beta_2} \quad (23)$$

$$B_{br,k} = \sum_{\alpha_1=1}^N \sum_{\beta_1=1}^{N_\alpha} W_\alpha W_{\alpha \beta} \bar{b}_{\alpha \beta}^{(k)} \beta_{\alpha \beta} \quad (24)$$

$$B_{br,k} = \sum_{\alpha_1=1}^N \sum_{\beta_1=1}^{N_\alpha} W_\alpha W_{\alpha \beta} L_{\alpha \beta}^k \beta_{\alpha \beta} \quad (25)$$

where the  $N$  primary weights  $W_\alpha$ , the corresponding primary abscissas  $L_\alpha$ , together with the parameter  $\sigma$  are determined from the first  $2N + 1$  integer moments of the NDF. The  $2N_\alpha$  quantities  $W_{\alpha \beta}$  and  $L_{\alpha \beta}$  called secondary weights and abscissas are computed using the standard Gaussian quadrature formulae for known orthogonal polynomials to the kernel NDF. The breakage kernel is shown by  $\beta_{\alpha \beta}$ , which is for the bubbles of size  $L_{\alpha \beta}$ .  $a_{\alpha_1 \beta_1 \alpha_2 \beta_2}$  is the aggregation kernel for the bubble size of  $L_{\alpha_1 \beta_1}$  and  $L_{\alpha_2 \beta_2}$ . The fragmentation distribution function is represented by  $\bar{b}_{\alpha \beta}$ , which is symmetric in the present work.

These equations have the form of the transport equations of a scalar variable in the dispersed phase and are solved using an open-source quadrature-based population balance solver for OpenFOAM (OpenQBMM). In the current work, two primary nodes and six secondary nodes have been chosen to apply the EQMOM method. A more detailed overview of the EQMOM method has been reported in the literature (Madadi-Kandjani and Passalacqua,<sup>[36]</sup> Gao et al.,<sup>[37]</sup> and Passalacqua et al.<sup>[45]</sup>).

#### Coalescence and break-up kernels

The choice of the coalescence and breakage kernels is a controversial issue in population balance modelling. At the moment there is little information in the literature stating which kernels can be chosen for different systems. It is recommended to examine their suitability and performance for each particular system. In the current investigation, the main focus has been given to general population balance framework (EQMOM) and mass transfer. Thus, the study of different breakage and coalescence functions left for our future work. In the present CFD model, the kernels are chosen based on the ones applied in the previous work for the same reactor and operational condition (Kerdouss et al.<sup>[8]</sup>).

#### • Break-up kernel

A break-up model by Luo and Svendsen,<sup>[46]</sup> derived from theories of isotropic turbulence, is used in this study. In a turbulent flow, bubble break-up occurs when eddies hit the bubbles surface with enough energy to overcome the surface tension. The bombarding eddies must be equal to or smaller than the bubble size as well. The model assumes the break-up is binary. The turbulent break-up mechanism can be modelled as the product of break-up probability and collision frequency. The probability is due to the energy contained in eddies and collisions happens between bubbles and turbulent eddies.

The individual rate breaking a parent bubble of size  $d_i$  into the daughter size classes  $d_j$  is expressed as:<sup>[47]</sup>

$$\Omega_{br}(d_i; d_j) = \int_{\lambda_{min}}^d \omega_{br}^T(d_i, \lambda) p_{br}(d_i; d_j, \lambda) d\lambda \quad \left( \frac{1}{sm^3} \right) \quad (26)$$

The eddy-bubble collision probability density  $\omega_{br}^T(d_i, \lambda)$  has units  $(1/sm^3 [m])$ . The upper integration limit for the eddy size is based on

the model assumption that only eddies of the size smaller than or equal to the bubble diameter can cause bubble breakage.<sup>[46]</sup>

The breakage density of one bubble of size  $d_i$  that breaks into bubbles of sizes  $d_j$  and  $(d_i^3 - d_j^3)^{1/3}$  is given by:<sup>[46]</sup>

$$\Omega_{br}(d_i: d_j) = 0.861 \alpha_L n_i \left( \frac{\epsilon}{d_i^2} \right)^{\frac{1}{3}} \int_{\xi_{min}}^1 \frac{(1 + \xi)^2}{\xi^{11/3}} \times \exp \left( - \frac{12 c_f \sigma}{2 \rho_L \epsilon^{2/3} d_i^{5/3} \xi^{11/3}} \right) d\xi \quad (27)$$

The increase energy in the surface area is obtained by:

$$c_f = f_{BV}^{2/3} + (1 - f_{BV}^{2/3})^{2/3} - 1 \quad (28)$$

where  $f_{BV}$  (= 0.5<sup>[46]</sup>) is breakage volume fraction which equals to  $\frac{\nu_j}{\nu_i}$ ,  $\xi$  is the ratio of eddy size to bubble size (dimensionless eddy size) when a bubble splits into two equal bubbles.

#### • Coalescence kernel

The coalescence rate is usually written as the product of collision rate  $\omega_{agr}(d_i, d_j)$  and coalescence efficiency  $p_c$ :

$$\Omega_{agr}(d_i: d_j) = \omega_{agr}(d_i: d_j) p_c(d_i: d_j) \quad (29)$$

The collision rate of bubbles per unit volume is given by Saffman and Turner<sup>[48]</sup> and can be written as:

$$\omega_{agr}(d_i: d_j) = 0.088 \pi n_i n_j (d_i + d_j)^2 \epsilon^{1/3} (d_i^{2/3} + d_j^{2/3})^{1/2} \quad (30)$$

where  $\epsilon$  is the turbulent energy dissipation rate per unit volume of liquid and  $d_i$  and  $d_j$  are the diameter of bubbles of abscissae i and j with their number density been given by  $n_i$  and  $n_j$ , respectively.

The coalescence probability of bubbles of sizes  $d_i$  and  $d_j$  is expressed as Luo and Svendsen.<sup>[46]</sup>

**Table 1.** Overview of mass transfer coefficients used in the model

Label	Theory	Correlation
(1)	Frossling	$Sh = 2 + 0.552 * Re^{0.5} * Sc^{0.33}$
(2)	Higbie	$Sh = 1.13 * Re^{0.5} * Sc^{0.5}$
(3)	Penetration Theory	$K_L = \frac{2}{\sqrt{\pi}} \sqrt{\frac{D_{O_2} U_{stip}}{d_{32}}}$
(4)	Surface Renewal Theory	$K_L = 0.4 \sqrt{D_{O_2}} \left( \frac{\epsilon_L}{v_L} \right)^{0.5}$

$$p_C(d_i, d_j) = \exp \left( -C \frac{[0.75(1 + \xi_{ij}^2)(1 + \xi_{ij}^3)]^{1/2}}{(\rho_d / \rho_c + 0.5)^{1/2} (1 + \xi_{ij})^3} We_{ij}^{1/2} \right) \quad (31)$$

where  $C = 0.5$ ,  $\eta_{ij} = \frac{d_i}{d_j}$ ,  $u_{ij} = (u_i^2 + u_j^2)^{1/2}$ ,  $u_i = \beta^{1/2} (\epsilon d_i)^{1/2}$ , and  $\beta = 2.05$ . In addition,  $u_i$  and  $u_j$  are bubble velocity and  $\sigma$  is surface tension.

#### Interphase Oxygen Mass Transfer

To model the interphase oxygen mass transfer, the oxygen transport equations are solved along with the phase mass, momentum and population balance equations. The transport equation for the local mass fraction of oxygen in the liquid phase is:

$$\begin{aligned} & \frac{\partial}{\partial t} (\rho_L \alpha_L Y_L O_2) + \nabla \cdot (\alpha_L \rho_L \vec{U}_L Y_L O_2) \\ &= \nabla \cdot \left( \alpha_L \left[ \rho_L D_{L,m} O_2 + \frac{\mu_t}{Sc_t} \right] \nabla Y_L O_2 \right) + K_L a (\rho_{L,e} O_2 - \rho_L O_2) \end{aligned} \quad (32)$$

where  $\rho_L$ ,  $D_{L,m} O_2$ ,  $Sc_t$ ,  $\rho_{L,e} O_2$ ,  $\rho_L O_2$ ,  $K_L$ , and  $a$  are the liquid phase density, the mass diffusion coefficient for oxygen in liquid phase, turbulent Schmidt number, equilibrium mass concentration of oxygen in water, mass concentration of oxygen in liquid phase, mass transfer coefficient, and interfacial area, respectively.

$\rho_{L,e} O_2$  is calculated by using Henry's Law as follows:

$$P_{O_2} = H \cdot \rho_{L,e} O_2 \quad (33)$$

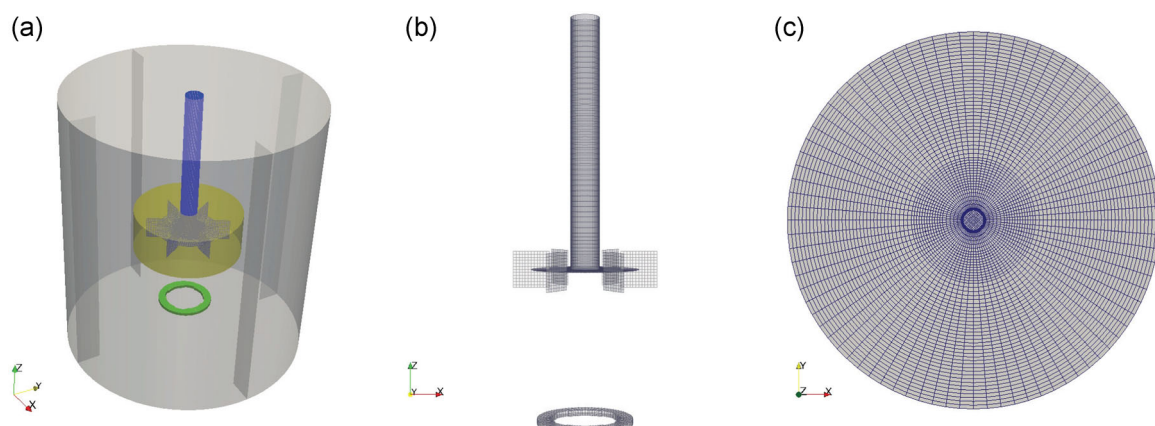


**Figure 1.** Schematic of Rushton turbine: (a) solution domain and MRF zone, (b) structured mesh in impeller and shaft with location of the sparger ring, and (c) front view of the structured mesh.

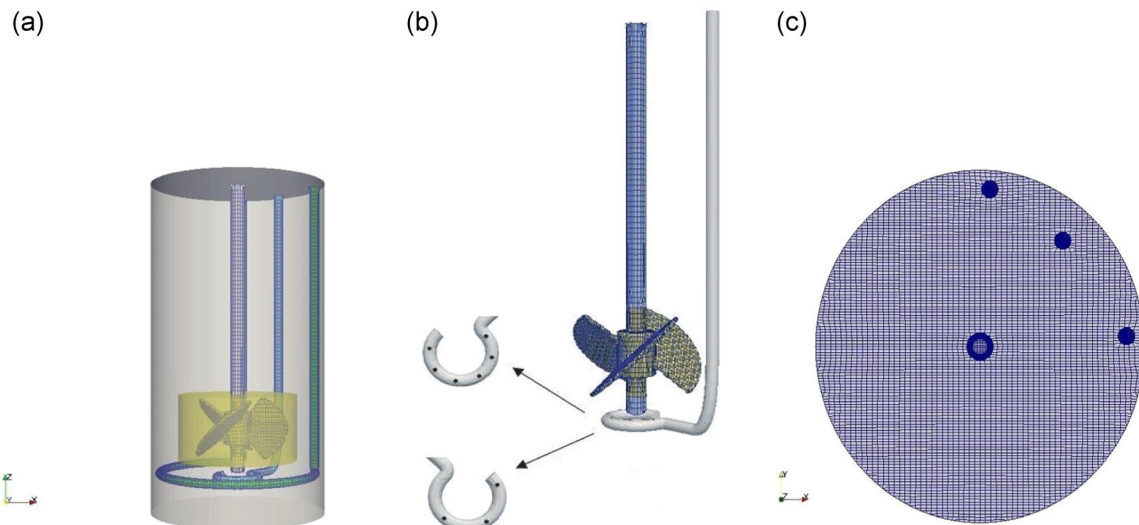


**Figure 2.** Schematic of bioreactor: (a) solution domain and MRF zone, (b) unstructured mesh in impeller and shaft with sparger location, and (c) front view of the unstructured mesh.

The Henry's constant and diffusion coefficient of oxygen at 20 °C, are respectively 4010 Pa kg<sup>-1</sup>m<sup>3</sup> and 2.01 × 10<sup>-9</sup>m<sup>2</sup>s<sup>-1</sup>. Using the CFD simulation, the volumetric mass transfer coefficient  $K_L a$  is calculated as the product of the liquid mass transfer coefficient  $K_L$  and the interfacial area  $a$ . Four theories for the mass transfer coefficient calculation are well known from the mass transfer literature, they are outlined in Table 1. The interfacial area is given as the function of the local gas volume fraction and local Sauter mean diameter  $d_{32}$ , which is computed by PBM:

$$a = \frac{6\alpha}{d_{32}} \quad (34)$$

#### TANK SPECIFICATIONS AND NUMERICAL TECHNIQUE

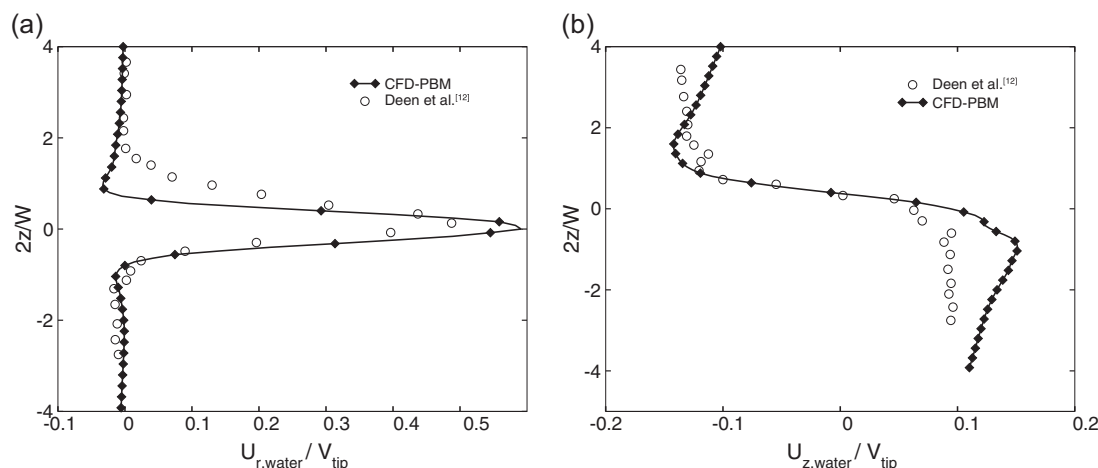
The solution domain is shown in Figures 1 and 2. BlockMesh as a toolbox of OpenFOAM is used for the first case and Salome and snappyHexMesh open source tools are used as the geometry and mesh generator in the second case.

Figure 1b and c demonstrates 446 341 hexahedral mesh in Rushton turbine. Figure 2b and c shows essential features of the

**Table 2.** The main characteristics of the test cases investigated in this study;  $\omega$ , the rotational speed (rpm) and  $K_L$ , the mass transfer coefficient (m/s)

Test cases	$\omega$	$Re$	$K_L$	Test cases	$\omega$	$Re$	$K_L$
Case 1	50	$3 \times 10^4$	(1)	Case 9	300	$17.63 \times 10^4$	(1)
Case 2	50	$3 \times 10^4$	(2)	Case 10	300	$17.63 \times 10^4$	(2)
Case 3	50	$3 \times 10^4$	(3)	Case 11	300	$17.63 \times 10^4$	(3)
Case 4	50	$3 \times 10^4$	(4)	Case 12	300	$17.63 \times 10^4$	(4)
Case 5	150	$8.8 \times 10^4$	(1)	Case 13	600	$35.2 \times 10^4$	(1)
Case 6	150	$8.8 \times 10^4$	(2)	Case 14	600	$35.2 \times 10^4$	(2)
Case 7	150	$8.8 \times 10^4$	(3)	Case 15	600	$35.2 \times 10^4$	(3)
Case 8	150	$8.8 \times 10^4$	(4)	Case 16	600	$35.2 \times 10^4$	(4)

482 422 cells generated for the bioreactor tank consisting of hexahedral, prisms, tetrahedral, and polyhedral. The final mesh resolution is based on Kerdouss et al.,<sup>[8]</sup> which allows us to consider 2–3 bubbles per computational cell.



**Figure 3.** Prediction of water axial ( $u_z$ ) and radial velocity ( $u_r$ ) at  $r/R = 0.37$  for the Rushton turbine.

**Table 3.** Overview of divergence schemes used in fvScheme dictionary

Variable	gas inlet (sparger)	outlet	shaft	impeller	walls
$\alpha_G$	1	zero grad.	zero grad.	zero grad.	zero grad.
$\vec{U}_G$	$U_{G,inlet}$	inletOutlet	rot. wall vel.	noSlip	noSlip
$\vec{U}_L$	0	inletOutlet	rot. wall vel.	noSlip	noSlip
$k_{L,G}$	$k_{inlet}$	inletOutlet	kqRWallFunc.	noSlip	noSlip
$\epsilon_{L,G}$	$\epsilon_{inlet}$	inletOutlet	epsilonWallFunc.	noSlip	noSlip
$m_i$	$m_{i,inlet}$	zero grad.	zero grad.	zero grad.	zero grad.
$Y_L O_2$	0	zero grad.	zero grad.	zero grad.	zero grad.

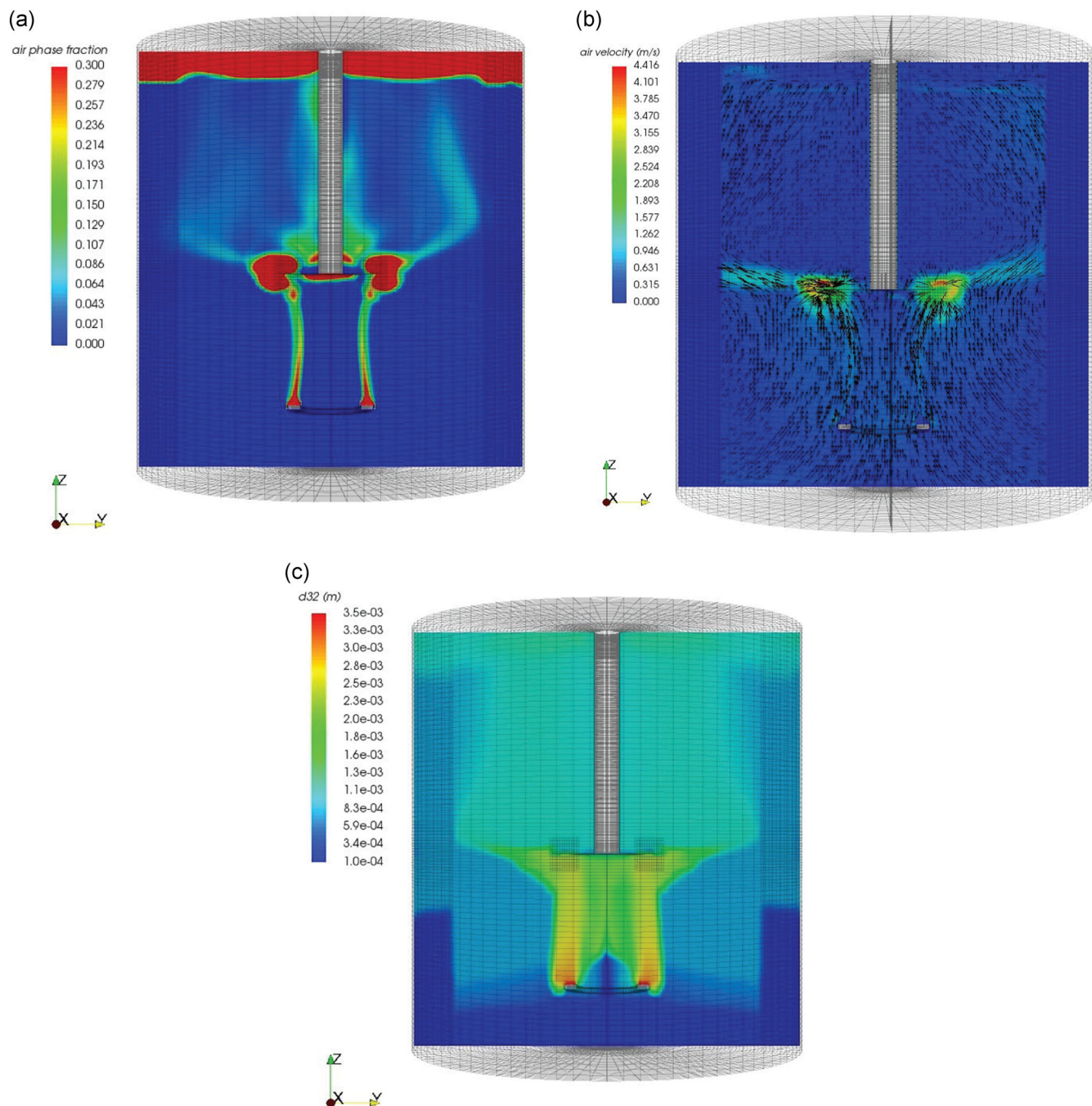


**Figure 4.** Contour map provided by CFD-PBM in Rushton reactor at  $\omega = 513$  rpm: (a) air phase fraction, (b) air velocity vectors, and (c) bubble size (Sauter diameter).

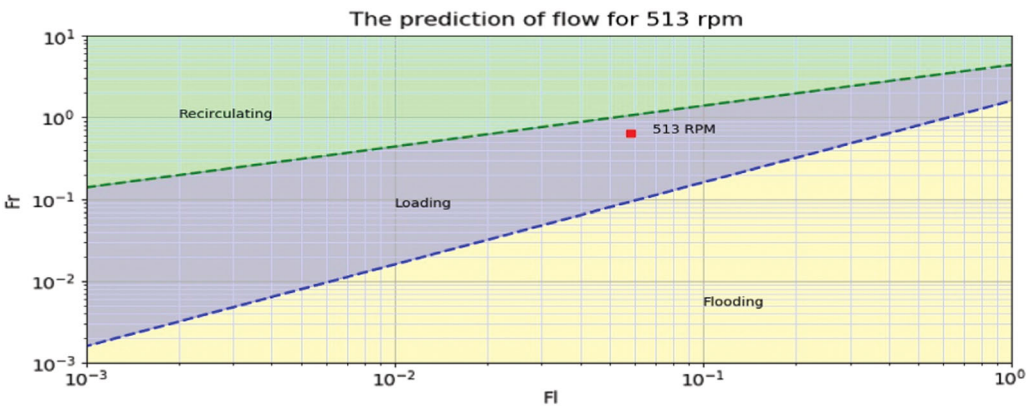


**Figure 5.** The flow condition in Rushton reactor based on Lee and Dudukovic<sup>[50]</sup> for  $\omega = 513$  rpm.

In this study, original reactingTwoPhaseEulerFoam solver of the Open source CFD code OpenFOAM-4.0 was used as a base to develop a new CFD-PBM solver called reactingTwoPhaseEulerQBMMFoam. First, the coalescence and breakage kernels and their connection with the turbulence model ( $k_{\text{water}}$  and  $\epsilon_{\text{water}}$ )

was developed in open quadrature-based moment methods (OpenQBMM).<sup>[45]</sup> Then OpenQBMM was fully integrated and coupled in reactingTwoPhaseEulerFoam. Next, the link between PBM and interfacial momentum exchange was established. Subsequently, the connection among mass transfer library ( $K_L$ ),

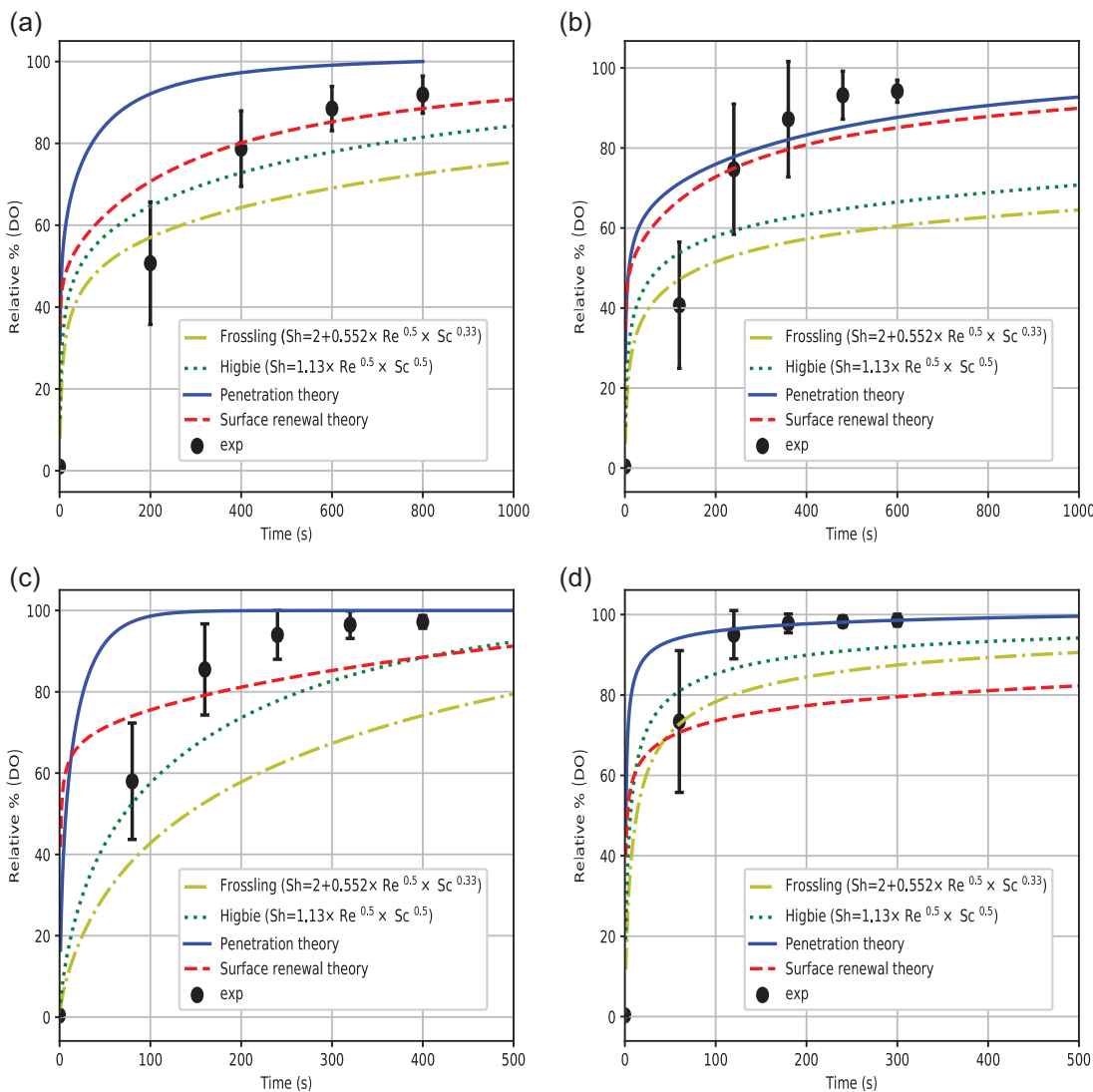


**Figure 6.** DO evolution for: (a)  $\omega = 50$  rpm, (b)  $\omega = 150$  rpm, (c)  $\omega = 300$  rpm, and (d)  $\omega = 600$  rpm.

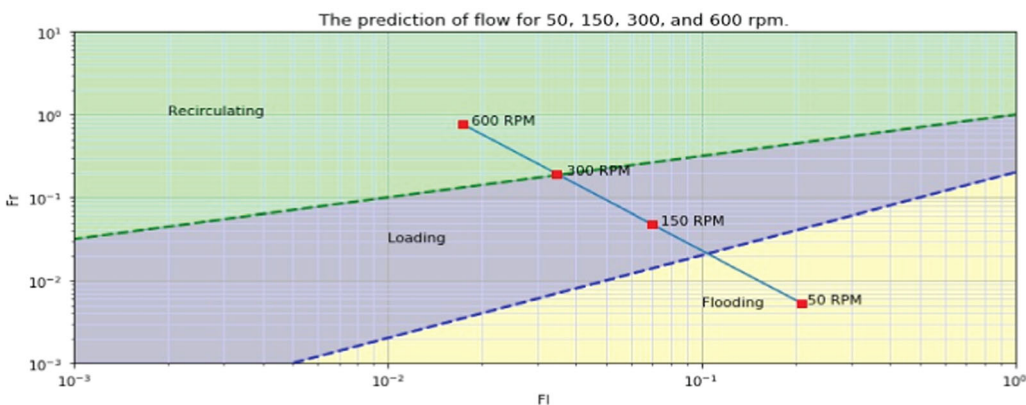


**Figure 7.** The flow condition in the bioreactor based on Lee and Dudukovic<sup>[50]</sup> for  $\omega = 50$ ,  $\omega = 150$ ,  $\omega = 300$ , and  $\omega = 600$  rpm.

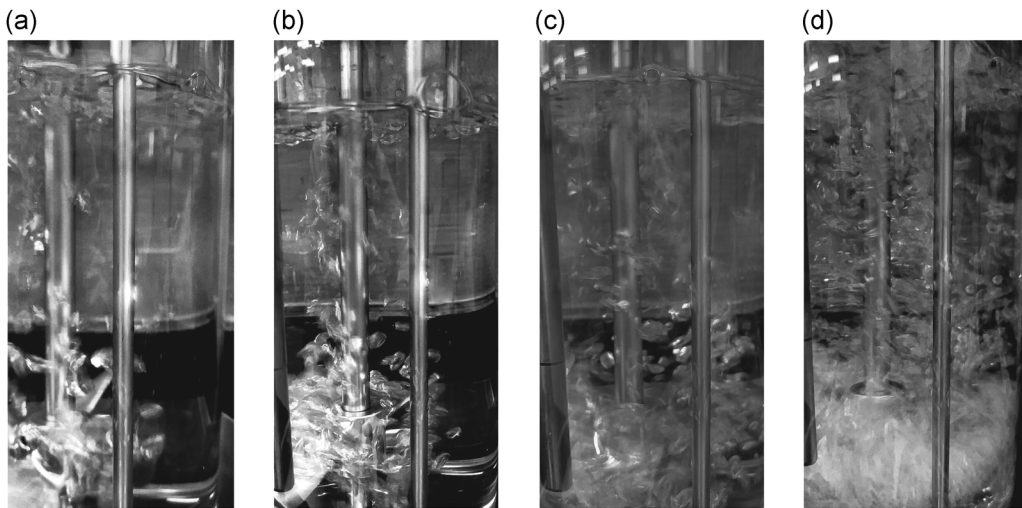


**Figure 8.** Experimental images in stirred tank for: (a)  $\omega = 50$  rpm, (b)  $\omega = 150$  rpm, (c)  $\omega = 300$  rpm, and (d)  $\omega = 600$  rpm.

PBM ( $d_{32}$ ) and turbulence ( $\epsilon$ ) was completed. To investigate the rotational speed of the impeller and mass transfer coefficient in the tank, the sixteen cases described in Table 2 were simulated.

The inlet velocity is calculated using the value of gas flow rate. The inlet gas volume fraction equals to unity since only gas is injected through inlet boundary. The bubble diameter at the sparger is assumed to be constant and its fixed value can be given by the following equation for low gas flow rates:<sup>[49]</sup>

$$d_b = \left( \frac{6\sigma d_o}{g(\rho_l - \rho_g)} \right)^{1/3} \quad (35)$$

where  $d_o$  is the orifice diameter.

For the simulation performed without the PBE model, the size of all bubbles inside the tank was determined by the same correlation. In this system, the orifices of the sparger are considered as inlet boundary. The shaft, as wall type boundary, separated from the impeller, is rotating. Thus, the velocity was configured in a cylindrical system. The angular component of shaft rotation is according to the rotational speed of impeller (rpm = 50–600).

An overview of the boundary conditions used in the system is shown in Table 3. Multiple reference frame model (MRF) is applied to consider the impeller region and make acceptable compromise between physical accuracy and affordable computational time. In fact, the main advantage of the MRF method is that there is no mesh motion involved. Modifying the mesh during the simulation is costly in terms of computational demand. To avoid numerical issues often seen in such complex multiphase equipments, the actual calculations started from the converged quasi steady-state with constant bubble size. In other words, converged quasi steady-state two-phase flow field with constant bubble size and MRF was used for the calculation of the steady-state two-phase flow with the MRF model and population balance model. Since our experimental observation shows the oxygen dissolution is a long-term process (between 500–3000 s), a shortcut strategy is adopted. The transient solver of mass transfer is launched with fixed fluid flow provided by steady-state solution of the solver coupling two-fluid model and population balance model. This method greatly accelerates the solution process and enable the user to reach the end time of water saturation. However, it cannot perfectly resolve the time-space evolution in early times of the saturation.

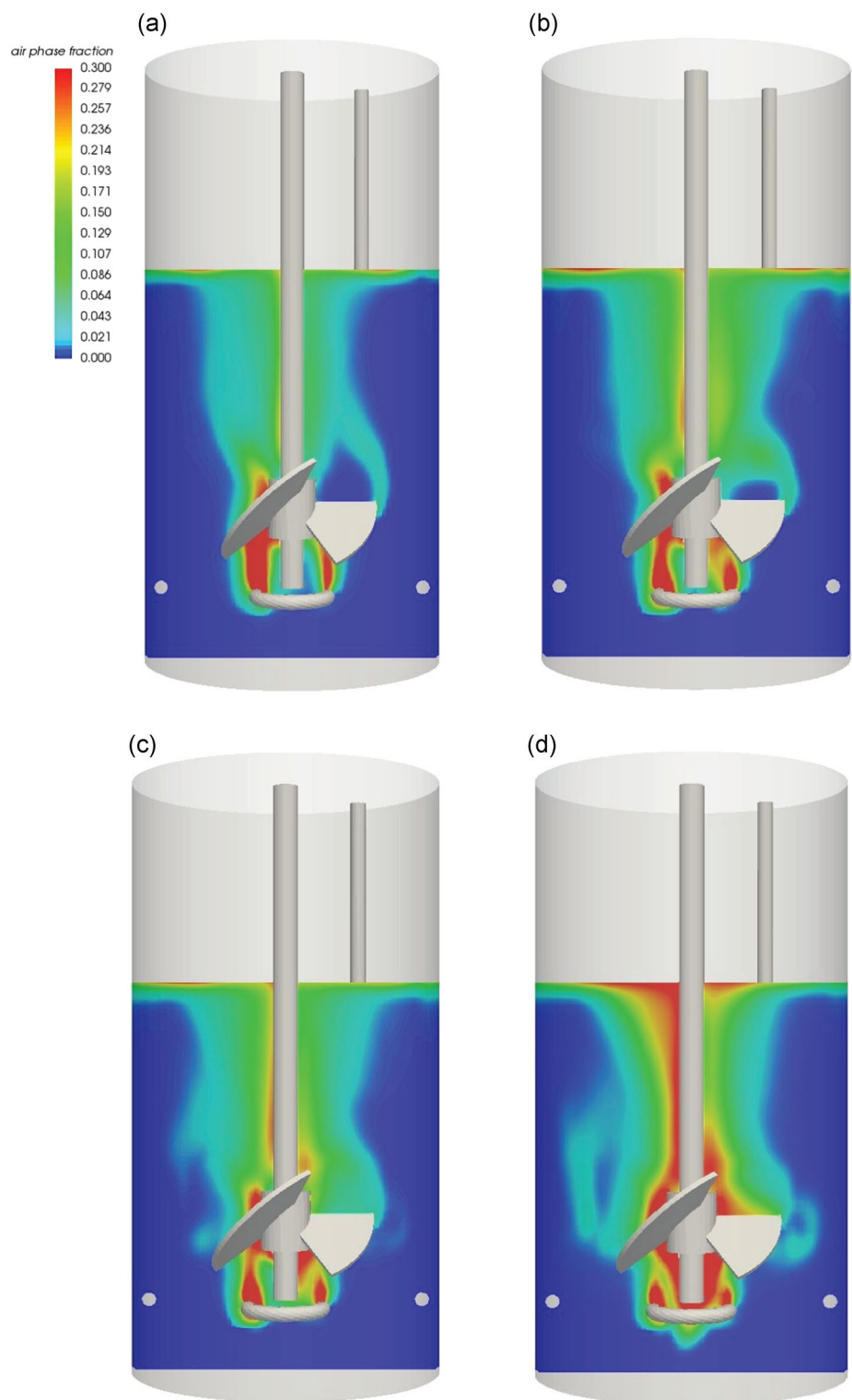


**Figure 9.** Contour of averaged-time gas hold-up along the plane located in the middle of the reactor: (a)  $\omega = 50$  rpm, (b)  $\omega = 150$  rpm, (c)  $\omega = 300$  rpm, and (d)  $\omega = 600$  rpm.

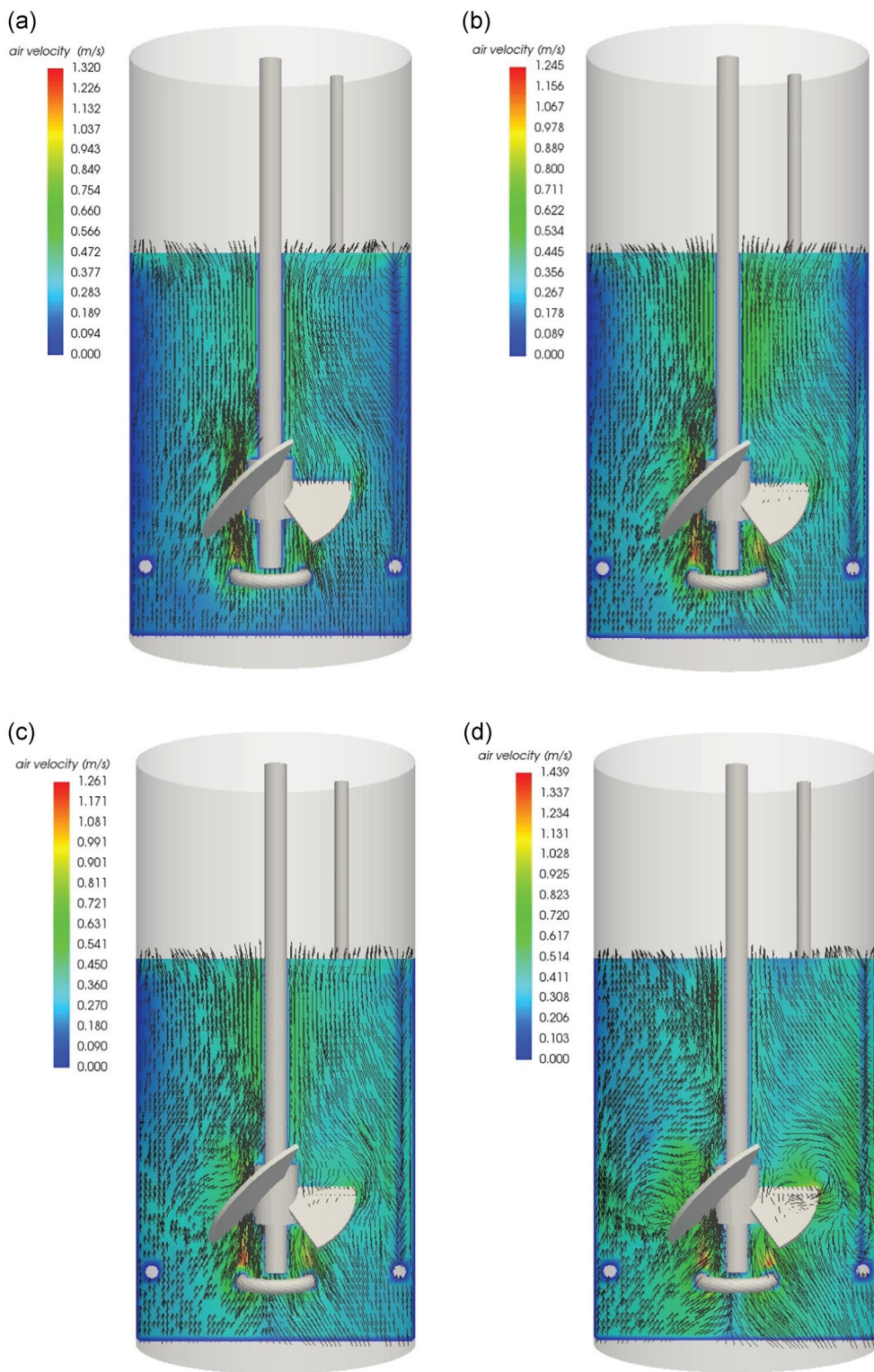


**Figure 10.** Averaged-time gas velocity vectors along the plane located in the middle of the reactor: (a)  $\omega = 50 \text{ rpm}$ , (b)  $\omega = 150 \text{ rpm}$ , (c)  $\omega = 300 \text{ rpm}$ , and (d)  $\omega = 600 \text{ rpm}$ .

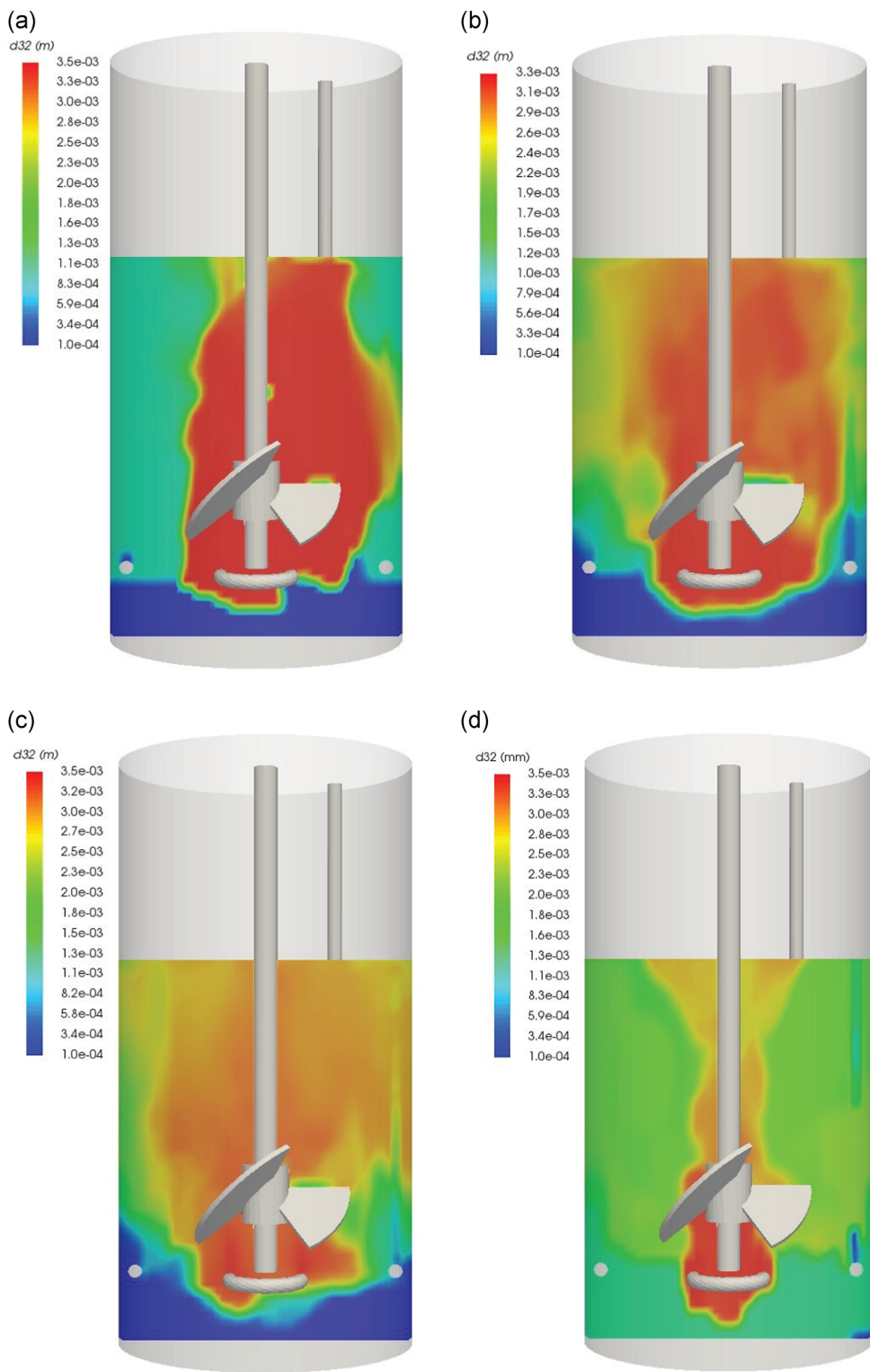


**Figure 11.** Contour of averaged-time local Sauter diameter along the plane located in the middle of the reactor: (a)  $\omega = 50$  rpm, (b)  $\omega = 150$  rpm, (c)  $\omega = 300$  rpm, and (d)  $\omega = 600$  rpm.

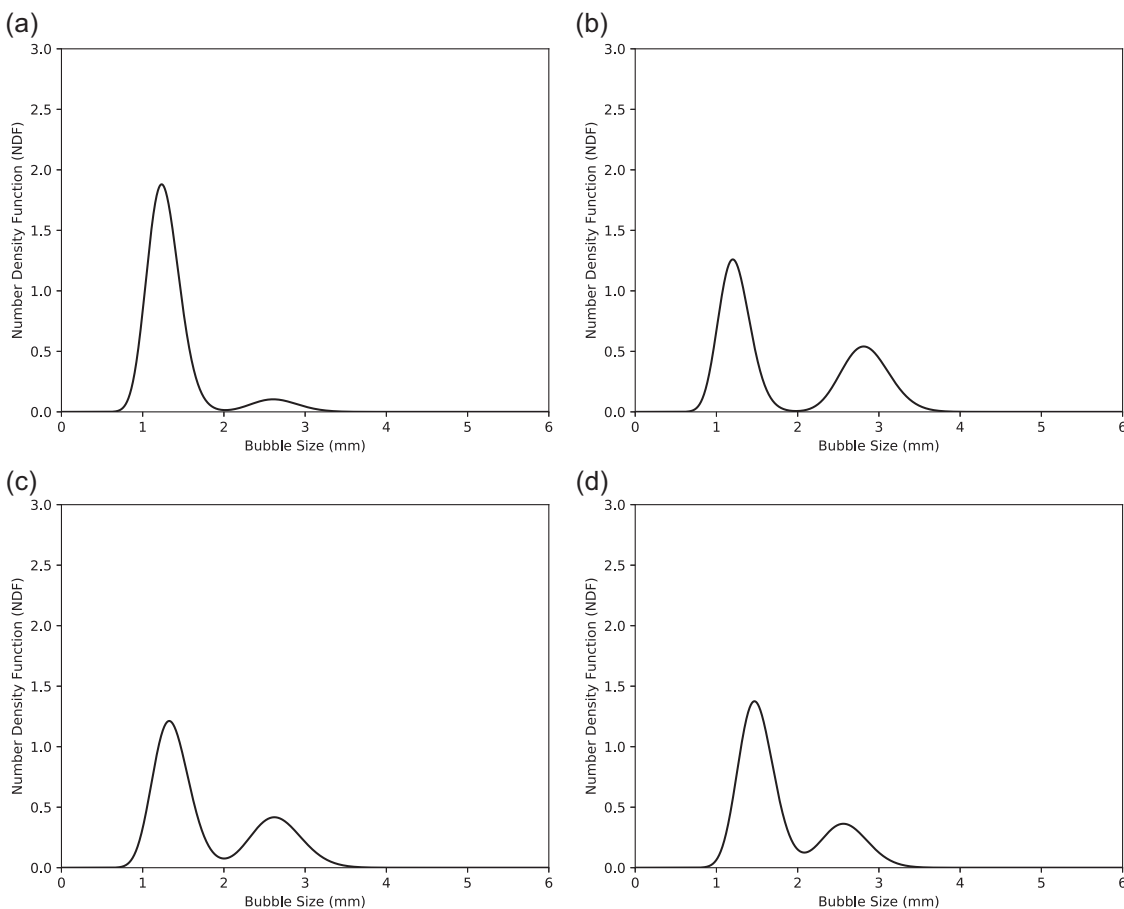


**Figure 12.** Dynamic number density function (NDF) in water zone for 50 rpm in: (a)  $\delta t = 1\text{s}$ , (b)  $\delta t = 2\text{s}$ , (c)  $\delta t = 3\text{s}$ , and (d)  $\delta t = 4\text{s}$ .

## RESULTS AND DISCUSSION

### Rushton Turbine

The time-averaged of axial and radial components of water velocity are compared with Deen et al.'s<sup>[12]</sup> PIV measurements. The results for the mean velocities were normalized using the impeller tip velocity ( $V_{tip}$ ). The results predicted by CFD-EQMOM modelling match slightly the experimental data (Figure 3).

Figure 4 shows the local gas hold-up, the gas velocity vectors and the local bubble sizes obtained by the CFD-PBM simulation for the Rushton stirred tank. The smallest bubbles can be observed around and above the impeller; whereas, the largest bubbles are found between the impeller and the sparger ring. The main reason for this event might be the combination of gas phase fraction and size of turbulent eddies. A large accumulation of the air phase is observed below the impeller. The dissipation rates in the regions close to impeller reach a maximum reducing the bubble size.

Figure 5 demonstrates that the 513 rpm case falls into the loading regime. This prediction was made using the Froude and the flow dimensionless numbers ( $\text{Fr} = \frac{N^2 D}{g}$  and  $\text{Fl} = \frac{Q_G}{ND^3}$ ).<sup>[50]</sup> The Froude number is the ratio of the impeller driven acceleration and gravity, and the flow number is the ratio of gas flow rate and impeller driven flow rate. The type of flow for the current exercise has been observed in simulation (Figure 4a and b) concerning the gas phase fraction and gas velocity vectors as well.

### New Brunswick Bioreactor

The developed CFD-PBM solver was used to simulate the gas-liquid stirred tank as presented in the Numerical Model section. Here, the validation process is carried out using the transient behaviour of oxygen concentration in the water due to lack of experimental information on the flow field.

The evolution of the dissolved oxygen concentration (DO) was tracked versus time using the transient solver of mass transfer with the fixed flow field and compared with the experimental measurements. Figure 6 illustrates the above-mentioned comparison for 50, 150, 300, and 600 rpm. The obtained results are nearly compatible with experimental measurements at the final period of time or close to complete saturation. In all cases, the shape of the dissolved oxygen concentration versus time is not well described in the first seconds. Experiments show a sigmoid curve followed by a rapid increase and concluded by a slow final increase. The primary cause of this discrepancy might be due to the chosen strategy (transient mass transfer with a fixed velocity field) to solve the equation of oxygen concentration.

As can be seen from Figure 6a-d, while a slight disagreement is found within initial minutes of oxygenation, a fair agreement is also observed using surface renewal theory in 50 rpm and penetration theory in 150, 300, and 600 rpm.

The presence of discrepancy observed in the model using surface renewal theory might be a result of the prediction of

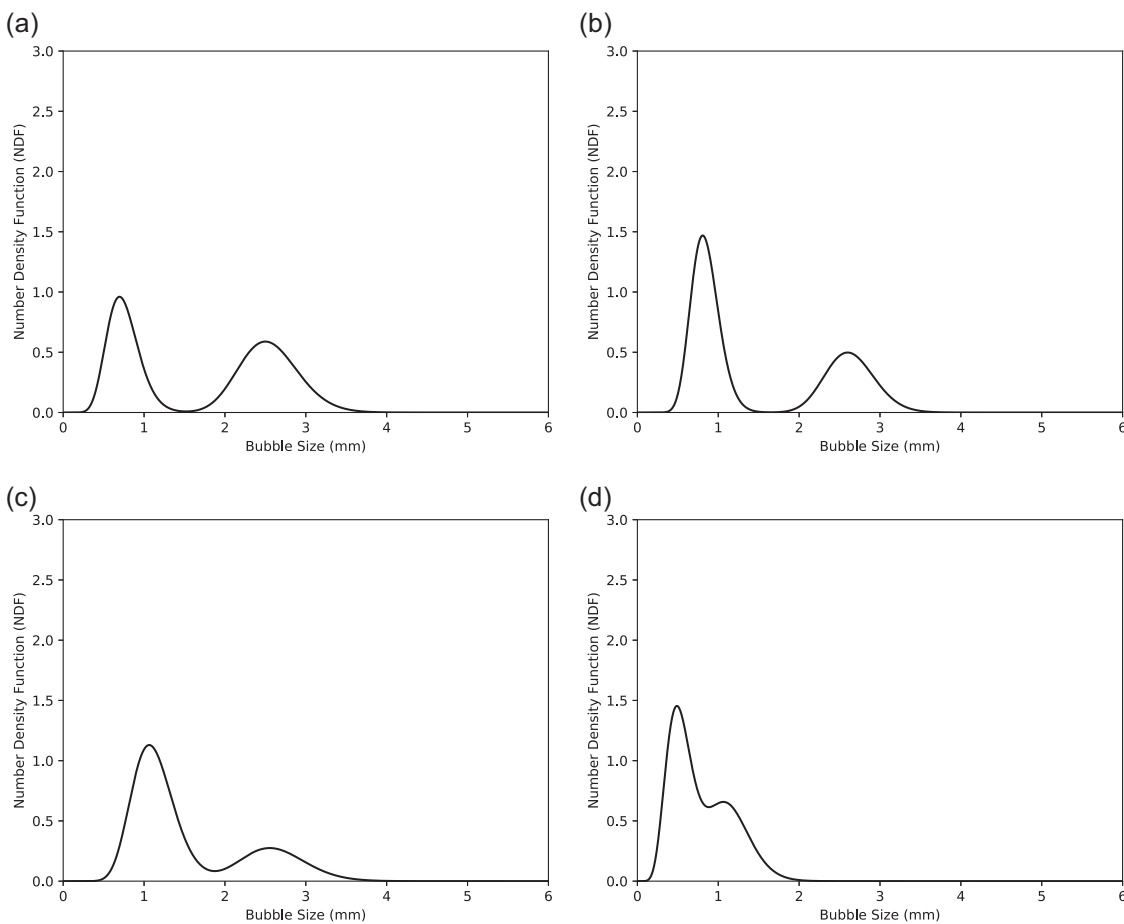


**Figure 13.** Dynamic number density function (NDF) in water zone for 150 rpm in: (a)  $\delta t = 1\text{s}$ , (b)  $\delta t = 2\text{s}$ , (c)  $\delta t = 3\text{s}$ , and (d)  $\delta t = 4\text{s}$ .

turbulence model which was coupled in the CFD-PBM solver. Since the key variable in the formulation of surface renewal theory is the turbulent kinetic energy dissipation rate ( $\epsilon$ ), the theory failed to predict the oxygen concentration in high turbulent cases. As has been shown in the literature, this problem is very common in the turbulent two-phase flows in mixers. Lane<sup>[51]</sup> has recently studied this shortcoming in the modelling of mixer tanks. According to his study, a fine and hybrid mesh can be used to overcome those difficulties.

As Figure 7 represents, the cases of 50, 150, 300, and 600 rpm fall into the flooding regime, loading regime, borderline of loading and recirculation, and recirculation regime, respectively. The type of flow for each exercise has been observed in the experiment (Figure 8) and simulation (Figures 9 and 10) considering gas phase fraction and gas velocity vectors.

As Figure 8 illustrates, the impeller speed increases from 50 to 600 rpm at a constant gas flow rate, the behaviour of the gas-liquid flow in the reactor has undergone considerable changes. Firstly, the gas sparging dominates and creates a bubble column type flow with gas rising in the centre. Next, the impeller begins to have an effect and then the circulation patterns of the stirred tank just begin to form. Finally, the circulation loops are partially developed and the impeller dominates the effects of the gas sparging. This similar transition can be predicted by the model which verifies the CFD-PBM solver, qualitatively. Figures 9 and 10 display time-averaged gas phase fraction and gas vector velocity in four different rotational speed through a vertical cut in the middle of the reactor.

In spite of the fact that increases in the rotational speed of the impeller lead to higher mixedness and air dispersion, it is still not enough to overcome the gas buoyancy. In the presence of the axial flow impeller, the gas bubbles rise near the shaft where shear forces are small, so that the flow pattern and discharging effect is disrupted. At 600 rpm, the gas dispersion is greater than other cases due to this fact that mixer power is greater than gas stream energy. However, the strong vortex caused by 600 rpm and water splash pull the injected air into the centre of the reactor and the rotating zone. These phenomena bring about more gas accumulation in the middle as well. By contrast (Figures 9d and 4), the air widely spread through the tank in the Rushton reactor with larger volume and lower rotation speed of the impeller. This issue will be discussed in one reactor with a different configuration of impellers in our future study.

Figure 11 exhibits the predicted contours of the local Sauter mean diameter in four different rotational speeds along the plane located in the middle of the tank. When the bubbles move upward and pass the impeller zone, the vortex caused by rotation of the impeller affects the bubbles. The strong eddies decrease the bubble size in the impeller region due to breakage event. This phenomenon becomes more intensive with a rise in rotational speed.

EQMOM is capable of reconstructing continuous number density function (NDF) for each arbitrary zone or any cell in a computational domain. This approach allows the acquiring of detailed information about dispersed phase and bubble particles. To plot the NDF, two weights and two abscissas ( $N = 2$ ) have to be calculated by EQMOM. The extracted values of weights and

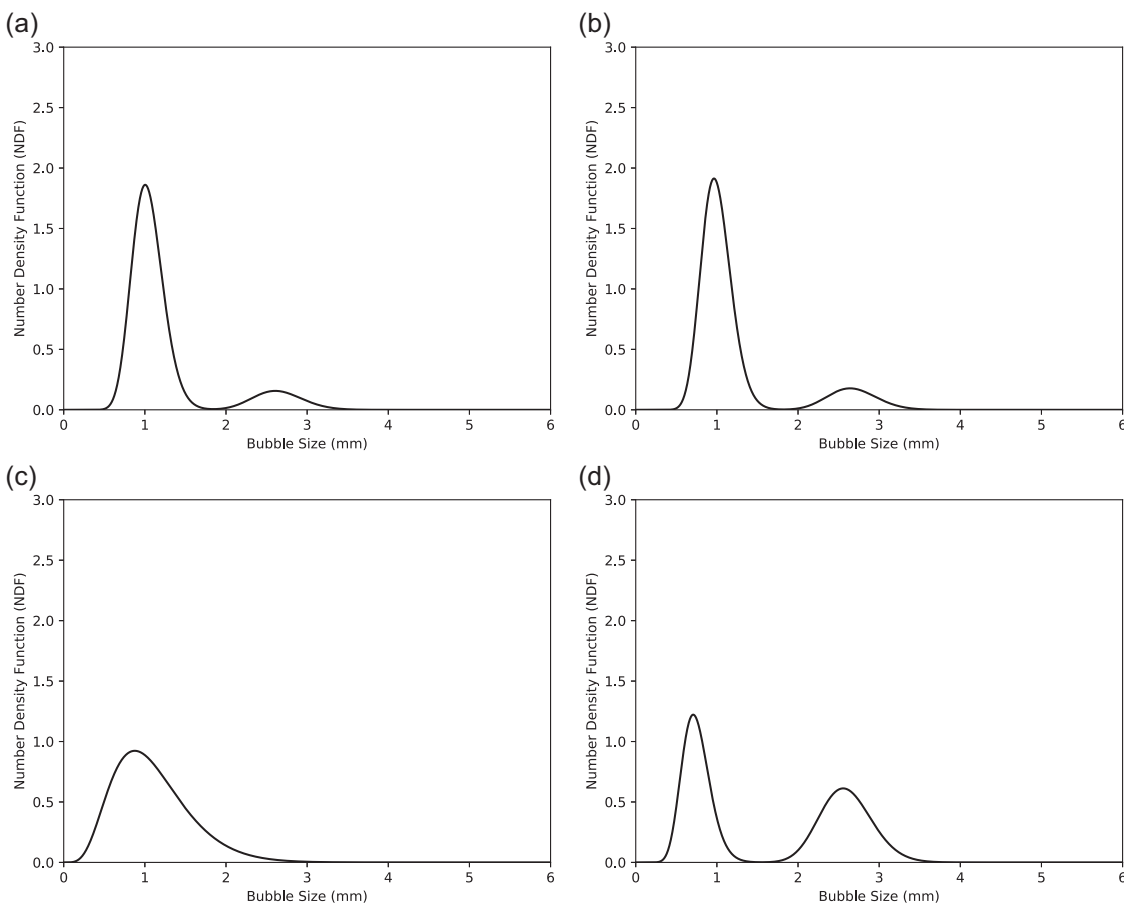


**Figure 14.** Dynamic number density function (NDF) in water zone for 300 rpm: (a)  $\delta t = 1\text{s}$ , (b)  $\delta t = 2\text{s}$ , (c)  $\delta t = 3\text{s}$ , and (d)  $\delta t = 4\text{s}$ .

abscissas from CFD-PBM solver are utilized to approximate Equation (20). Figures 12–15 indicate one of the possible shapes of the NDF in the liquid phase (water zone) corresponding to the considered moments for a four-second period after the achievement of quasi steady-state condition (excluding mass transfer) in the system for different rotational speed of the impeller. To achieve the continuous NDF the average moments through the entire domain was computed and then the spectrum of NDF was reconstructed based on the averaged moments.

The reason behind the use of PBM is to capture the physics of the problem accurately. The size distribution shows bubbles with different mean values. The mean bubble diameter ranges from 0.1–4 mm and the monodispersity is not a good approximation. As can be observed from Figures 12–15, the NDF is bimodal for the 50 and 150 rpm cases and practically for 300 rpm. This might be due to the limited interaction among bubbles and between bubbles and the continuous phase. In these cases, the energy is limited to mixer action. This input is not strong enough to create a smooth trend in the NDF. It was observed that there is only one snapshot in 300 rpm that exhibits a unimodal distribution. As Figure 15 demonstrates, the spectrum was totally converted into unimodal distribution and the bimodal trend has disappeared at 600 rpm. This is because of the energy which is spread out through the flow field by the gas stream and the mixer. The released energy generates strong eddies, which result in more coalescence and breakage among bubbles compared to the lower speed of the impeller. Another reason might be due to the presence of large polydispersity in high turbulent cases.

## CONCLUSION

In this paper, a study was carried out for two aerated stirred tanks, called the Rushton turbine and bioreactor, containing axial and radial impellers, respectively. The CFD-PBM solver which can be applied for a stirred tank to predict the bubble size distribution and local oxygen mass concentration in water was fairly validated by the results obtained. The originality of the OpenFOAM solver lies in EQMOM application as a PBM model. The implemented PBM can accept the continuous bubble size distribution as the boundary condition and is able to export a distribution function for a specified region in an arbitrary time. For the first time, the described model has been carried out in a stirred tank reactor including gas-liquid flow agitated by an axial impeller. The study of the bioreactor shows that the two-phase mass transfer model using surface renewal theory obtains superior predictions (DO) for 50 rpm (the lowest rotational speed of impeller in this study for bioreactor). However, the model using penetration theory appears to be more appropriate (DO) for 150, 300, and 600 rpm. From the numerical results, it is evident the NDF is bimodal for 50, 150, and nearly 300 rpm and unimodal for 600 rpm. The proposed model also shows that the prediction of (DO) have a slight discrepancy in early times between the numerical results and experimental data. This aspect of the model should be further investigated by improving the applied transient strategy, the validation of the bubble size distribution, and turbulent dissipation rates. The model demonstrates that the use of an axial impeller in aerated tanks is not satisfactory and the use of a Rushton agitator is more efficient for more gas dispersion.

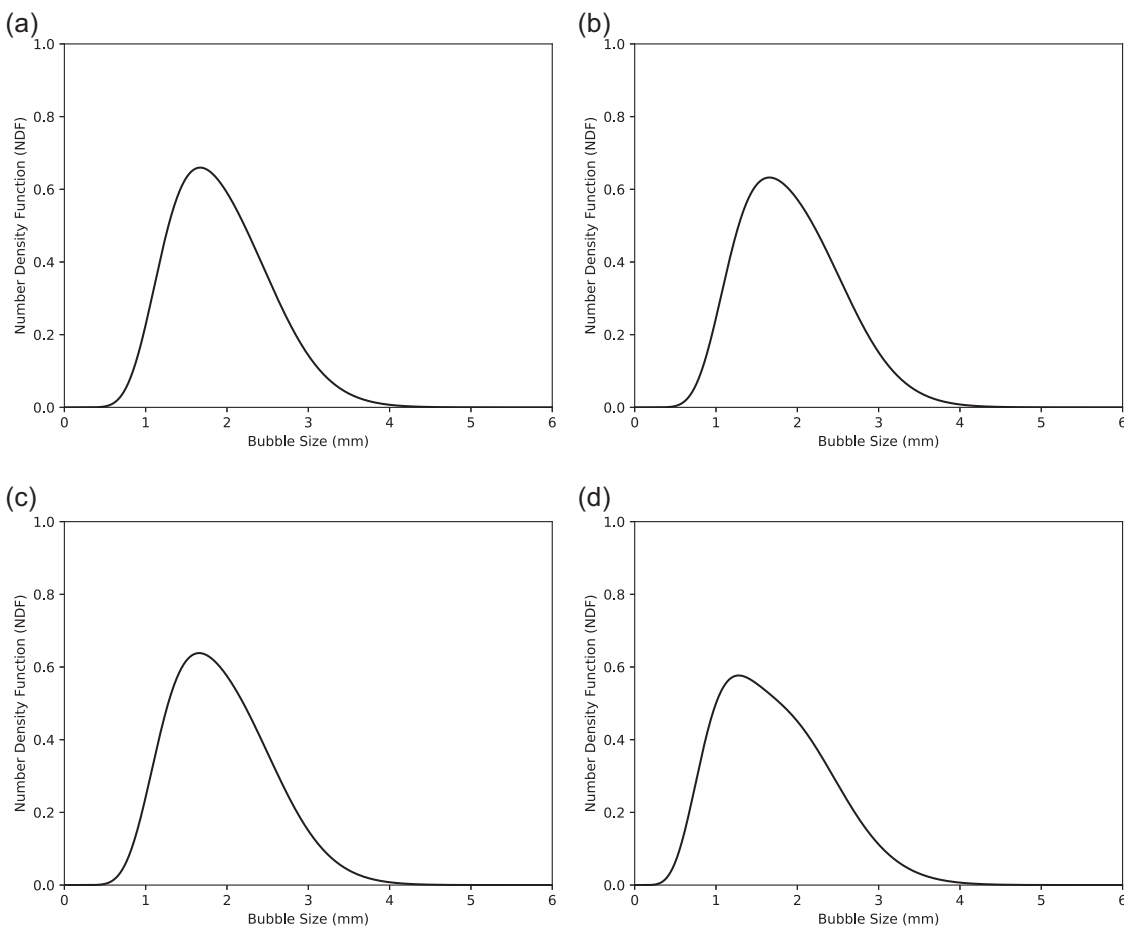


**Figure 15.** Dynamic number density function (NDF) in water zone for 600 rpm: (a)  $\delta t = 1\text{s}$ , (b)  $\delta t = 2\text{s}$ , (c)  $\delta t = 3\text{s}$ , and (d)  $\delta t = 4\text{s}$ .

## ACKNOWLEDGEMENT

The authors would like to thank the Hydro-Québec Research Center (IREQ) and NSERC for financially supporting this study.

## NOMENCLATURE

$a$	interfacial area ( $\text{m}^{-1}$ )
$C_D$	drag coefficient
$c_f$	increase coefficient of surface area
$D^{O_2}$	oxygen diffusion coefficient ( $\text{mm}^2 \cdot \text{s}^{-1}$ )
$d$	bubble diameter (m)
$d_o$	sparger orifice (m)
$d_{32}$	Sauter mean diameter (m)
$Eo$	Eotvos number
$\vec{F}$	volumetric force ( $\text{N} \cdot \text{m}^{-3}$ )
$\vec{g}$	acceleration vector due to gravity ( $\text{m} \cdot \text{s}^{-2}$ )
$H$	Henry's constant ( $\text{Pa} \cdot \text{kg}^{-1} \cdot \text{m}^3$ )
$\bar{\mathbb{I}}$	unit tensor
$k$	turbulent kinetic energy ( $\text{J} \cdot \text{kg}^{-1}$ )
$K$	exchange coefficient ( $\text{kg} \cdot \text{m}^{-3} \cdot \text{s}^{-1}$ )
$K_L$	mass transfer coefficient ( $\text{m} \cdot \text{s}^{-1}$ )
$N$	angular velocity ( $\text{rad} \cdot \text{s}^{-1}$ )
$p$	pressure (Pa)
$p_c$	coalescence efficiency or collision probability

$P_{O_2}$	partial pressure of oxygen (Pa)
$R$	vessel diameter of Rushton reactor (m)
$\vec{r}$	position vector (m)
$\vec{R}$	interphase force ( $\text{N} \cdot \text{m}^{-3}$ )
$Re$	Reynolds number
$\bar{R}_\phi^{eff}$	Reynolds (turbulent) and viscous stress ( $\text{m} \cdot \text{s}^{-2}$ )
$Sc$	Schmidt number
$Sh$	Sherwood number
$t$	time (s)
$\vec{U}$	average velocity of phase ( $\text{m} \cdot \text{s}^{-1}$ )
$u_{ij}$	bubble approaching turbulent velocity ( $\text{m} \cdot \text{s}^{-1}$ )
VVM	volume per unit volume
$W$	impeller blade width (m)
$Y^{O_2}$	local mass fraction of oxygen

## Greek Symbols

$\alpha$	volume fraction
$\beta$	constant (2.05)
$\epsilon$	turbulent kinetic energy dissipation rate ( $\text{m}^2 \cdot \text{s}^{-3}$ )
$\mu$	dynamic viscosity of the continuous phase ( $\text{N} \cdot \text{m}^{-3}$ )
$\lambda$	eddy size (m)
$\rho$	density ( $\text{kg} \cdot \text{m}^{-3}$ )
$\rho^{O_2}$	oxygen mass concentration ( $\text{kg} \cdot \text{m}^{-3}$ )
$\sigma$	surface tension ( $\text{N} \cdot \text{m}^{-1}$ )

$\zeta$	internal variable
$\xi$	dimensionless eddy size ( $\lambda/d_j$ )
$\Gamma$	incomplete Gamma function
$\eta$	diameter ratio ( $d_i/d_j$ )

## Subscripts

agr	aggregation
br	breakage
eff	effective
G	gas phase
i	phase number
L	liquid phase
lam	laminar
t	turbulent

## REFERENCES

- [1] J. Y. Luo, R. I. Issa, A. D. Gosman, *IChemE Symposium Series* **1994**, *136*, 549.
- [2] G. Tabor, A. D. Gosman, R. I. Issa, *IChemE Symposium Series* **1996**, *140*, 25.
- [3] G. Micale, A. Brucato, F. Grisafi, *AICHE J.* **1999**, *45*, 445.
- [4] G. Holzinger, *Eulerian Two-Phase Simulation of the Floating Process with OpenFOAM*, PhD thesis, Johannes Kepler Universität Linz, Linz **2016**.
- [5] G. L. Lane, M. P. Schwarz, G. M. Evans, *Chem. Eng. Sci.* **2005**, *60*, 2203.
- [6] B. C. H. Venneker, J. J. Derksen, H. E. A. VanDenAkker, *AICHE J.* **2002**, *48*, 673.
- [7] F. Kerdouss, A. Bannari, P. Proulx, *Chem. Eng. Sci.* **2006**, *61*, 3313.
- [8] F. Kerdouss, A. Bannari, P. Proulx, *Comput. Chem. Eng.* **2007**, *32*, 1943.
- [9] F. Kerdouss, L. Kiss, P. Proulx, J. F. Bilodeau, C. Dupuis, *Int. J. Chem. React. Eng.* **2005**, *3*, A35.
- [10] G. L. Lane, M. P. Schwarz, G. M. Evans, *Appl. Math. Model.* **2002**, *26*, 223.
- [11] J. Gimbut, C. D. Rielly, Z. K. Nagy, *Chem. Eng. Res. Des.* **2009**, *87*, 437.
- [12] N. G. Deen, T. Solberg, B. H. Hjertager, *Can. J. Chem. Eng.* **2002**, *80*, 1.
- [13] P. C. Friberg, *Three-Dimensional Modeling and Simulations of Gas-Liquid Flows Processes in Bioreactors*, PhD thesis, Norwegian University of Science and Technology, Trondheim **1998**.
- [14] K. E. Morud, B. H. Hjertager, *Chem. Eng. Sci.* **1996**, *51*, 233.
- [15] V. V. Ranade, V. R. Deshpande, *Chem. Eng. Sci.* **1999**, *54*, 2305.
- [16] V. V. Ranade, *Chem. Eng. Sci.* **1997**, *52*, 4473.
- [17] S. M. Kresta, A. W. Etchells III, D. S. Dickey, V. A. Atiemo-Obeng, *Advances in Industrial Mixing*, Wiley, Hoboken **2015**.
- [18] M. Ishii, S. Kim, J. Uhle, *Int. J. Heat Mass Tran.* **2002**, *45*, 3111.
- [19] K. Dhanasekharan, J. Sanyal, A. Jain, A. Haidari, *Chem. Eng. Sci.* **2005**, *60*, 213.
- [20] B. V. Balakin, A. C. Hoffmann, P. Kosinski, *Powder Technol.* **2014**, *257*, 47.
- [21] R. Bannari, F. Kerdous, B. Selma, A. Bannari, P. Proulx, *Comput. Chem. Eng.* **2008**, *32*, 3224.
- [22] P. J. Becker, F. Puel, R. Henry, N. Sheibat-Othman, *Ind. Eng. Chem. Res.* **2011**, *50*, 11358.
- [23] S. Kumar, D. Ramkrishna, *Chem. Eng. Sci.* **1996a**, *51*, 1311.
- [24] S. Kumar, D. Ramkrishna, *Chem. Eng. Sci.* **1996b**, *51*, 1333.
- [25] F. Puel, G. Fvotte, J. P. Klein, *Chem. Eng. Sci.* **2003**, *58*, 3715.
- [26] R. McGraw, *Aerosol Sci. Tech.* **1997**, *27*, 255.
- [27] D. L. Marchisio, R. D. Vigil, R. O. Fox, *J. Colloid Interf. Sci.* **2003a**, *258*, 322.
- [28] D. L. Marchisio, J. T. Pikturna, R. O. Fox, R. D. Vigil, *AICHE J.* **2003b**, *49*, 1266.
- [29] D. L. Marchisio, R. D. Vigil, R. O. Fox, *Chem. Eng. Sci.* **2003c**, *139*, 3337.
- [30] J. Sanyal, D. L. Marchisio, R. O. Fox, K. Dhanasekharan, *Ind. Eng. Chem. Res.* **2005**, *44*, 5063.
- [31] L. Silva, P. Lage, *Comput. Chem. Eng.* **2011**, *35*, 2653.
- [32] B. Selma, R. Bannari, P. Proulx, *Chem. Eng. Sci.* **2010**, *65*(6), 1925.
- [33] D. L. Marchisio, R. O. Fox, *J. Aerosol Sci.* **2004**, *36*, 43.
- [34] Y. Liao, R. Oertel, S. Kriebitzsch, F. Schlegel, D. Lucas, *Int. J. Numer. Meth. Fl.* **2018**, *87*, 202.
- [35] C. Yuan, F. Laurant, R. O. Fox, *J. Aerosol Sci.* **2012**, *51*, 1.
- [36] E. Madadi-Kandjani, A. Passalacqua, *Chem. Eng. Sci.* **2015**, *131*, 323.
- [37] Z. Gao, D. Li, A. Buffo, W. Podgrska, D. L. Marchisio, *Chem. Eng. Sci.* **2016**, *142*, 277.
- [38] D. Li, Z. G. A. Buffo, W. Podgrska, D. L. Marchisio, *AICHE J.* **2017**, *63*, 2293.
- [39] E. Askari, P. Proulx, A. Passalacqua, *ChemEngineering* **2018**, *2*, 8.
- [40] F. Scargiali, A. d'Orazio, F. Grisafi, A. Brucato, *Chem. Eng. Res. Des.* **2007**, *85*, 637.
- [41] A. Tomiyama, I. Kataoka, I. Zun, T. Sakaguchi, *JSME Int. J.* **1998**, *41*, 472.
- [42] A. Bakker, H. E. A. VanDenAkker, *Trans. Inst. Chem. Eng.* **1994**, *72*(A), 594.
- [43] B. Behzadi, R. I. Issa, H. Rusche, *Chem. Eng. Sci.* **2004**, *59*, 759.
- [44] M. Vanni, *J. Colloid Interf. Sci.* **1999**, *221*, 143.
- [45] A. Passalacqua, F. Laurent, E. Madadi-Kandjani, J. Heylmun, R. Fox, *Chem. Eng. Sci.* **2018**, *176*, 306.
- [46] H. Luo, H. F. Svendsen, *AICHE J.* **1996**, *42*, 1225.
- [47] H. A. Jakobsen, *Chemical Reactor Modelling*, Verlag, Berlin, **2008**.
- [48] P. G. Saffman, J. S. Turner, *J. Fluid Mech.* **1956**, *1*, 16.
- [49] M. Moo-Young, H. W. Blanch, *Adv. Biochem. Eng.* **1981**, *19*, 1.
- [50] B. W. Lee, M. P. Dudukovic, *Chem. Eng. Sci.* **2014**, *109*, 264.
- [51] G. L. Lane, *Chem. Eng. Sci.* **2017**, *169*, 188.

Manuscript received June 2, 2018; revised manuscript received August 15, 2018; accepted for publication September 13, 2018.